BioOne COMPLETE

Rapid, Remote Assessment of Hurricane Matthew Impacts Using Four-Dimensional Structure-from-Motion Photogrammetry

Authors: Sherwood, Christopher R., Warrick, Jonathan A., Hill, Andrew D., Ritchie, Andrew C., Andrews, Brian D., et al.

Rapid, Remote Assessment of Hurricane Matthew Impacts Using Four-Dimensional Structure-from-Motion Photogrammetry

Christopher R. Sherwood[†]*, **Jonathan A. Warrick**[‡], **Andrew D. Hill**[‡], **Andrew C. Ritchie**[‡], **Brian D. Andrews**[†], and **Nathaniel G. Plant**[§]

[†]Woods Hole Coastal and Marine Science Center
U.S. Geological Survey
Woods Hole, MA 02543, U.S.A.

[‡]Pacific Coastal and Marine Science Center
U.S. Geological Survey
Santa Cruz, CA 95060, U.S.A.

[§]St. Petersburg Coastal and Marine Science Center
U.S. Geological Survey
St. Petersburg, FL 33701, U.S.A.

www.JCRonline.org

ABSTRACT

Sherwood, C.R.; Warrick, J.A.; Hill, A.D.; Ritchie, A.C.; Andrews, B.D., and Plant, N.G., 2018. Rapid, remote assessment of Hurricane Matthew impacts using four-dimensional structure-from-motion photogrammetry. *Journal of Coastal Research,* 34(6), 1303–1316. Coconut Creek (Florida), ISSN 0749-0208.

Timely assessment of coastal landforms and structures after storms is important for evaluating storm impacts, aiding emergency response and restoration, and initializing and assessing morphological models. Four-dimensional multiview photogrammetry, also known as structure from motion (4D SfM), provides a method for generating three-dimensional reconstructions of landscapes at two times (before and after events) using only photos and existing information for ground control points. Here, these techniques were applied using National Oceanic and Atmospheric Administration (NOAA)-obtained oblique aerial photos taken before (2015) and immediately after Hurricane Matthew (2016) to assess coastal changes near Matanzas, Florida. This work demonstrated that 3D digital elevation models can be constructed within 48 hours of postevent photo collection without on-site ground control measurements. One advantage of timely SfM elevation-change assessments is that they avoid confusion of storm impacts with changes that occur after the event but before LIDAR surveys can be performed. The accuracy and precision of the 4D SfM maps were assessed *a posteriori* using the first-available LIDAR data, which were collected more than a month after the hurricane, and 11 independent ground-truth survey points measured a week after the hurricane. Horizontal coordinates of the 4D SfM reconstruction were biased by an average of 0.79 m (0.83 m root-mean-square difference; RMSD) compared with the ground-truth points, but vertical elevations were more accurate. They were biased from the LIDAR by –0.09 to –0.25 m, with ∼0.20 m RMSD from both the LIDAR data and five ground-truth points with good vertical positioning and 0.25 m RMSD from LIDAR data along a 60-m stretch of pavement. This level of precision was sufficient to quantify geomorphological change that was often in excess of 1 m. The methodology is conducive for rapid assessment of changes along short stretches (tens of kilometers) of coast with modest resources and could be scaled up for larger regions.

ADDITIONAL INDEX WORDS: *Coastal geomorphology, coastal monitoring, remote sensing, multiview stereo photogrammetry, oblique aerial photography.*

INTRODUCTION

This section describes the need for timely, quantitative maps of conditions following coastal storms and reviews approaches for obtaining coastal change measurements. This section also outlines the objectives of this paper, introduces the study area near Matanzas, Florida, and describes the oceanographic conditions associated with Hurricane Matthew.

Motivation

Timely assessment of coastal changes following storms is important for emergency response and planning recovery operations. Access is often limited in coastal regions after storms, so remote sensing methods can provide scientists, first responders, and local and federal resource and emergency

management authorities with information about flooding, road conditions, and damage to habitat or infrastructure.

Forecasts of storm impacts begin with a prestorm beach landscape, usually based on LIDAR measurements (*e.g.*, Stockdon, Doran, and Sallenger, 2009). The actual changes to beaches during storms can be influenced by the prestorm beach state, in addition to the oceanographic and geologic conditions during the storm (*e.g.*, Angnuureng *et al.*, 2017; Barnard *et al.*, 2014; Yates, Guza, and O'Reilly, 2009). Changes to beach morphology during storms, especially the formation of breaches or the closing of existing inlets, may leave the coast in a more vulnerable condition, so, ideally, forecasts for subsequent storms should use an updated beach state. Updates may be particularly important during hurricane season or an El Niño winter, when storms are prolonged, slow-moving, or occur in rapid succession, for example during Hurricane Matthew in 2016 (Stewart, 2017) or Hurricanes Irma and Jose in 2017, or the El Niño of 2015–16 (Barnard *et al.*, 2017). However, the ability to measure and update the beach state after a storm for

immediate use in new forecasts requires rapid, quantitative measurements of the new beach morphology.

Measurements of immediate poststorm conditions are also essential to researchers for development and evaluation of models of coastal change and flooding in response to storms. The utility of LIDAR to conduct measurement for storm response has been evaluated previously (Brock *et al.*, 2002; Stockdon, Doran, and Sallenger, 2009). Owing to the high cost of LIDAR equipment and processing, acquisition requires planning and investment that, typically, takes a week after a storm impacts the coast (Sopkin *et al.*, 2014). The morphology that exists during and immediately following a storm can be modified by natural processes and human recovery activities in the days and weeks after the event, obscuring the effects of any particular storm (Lindemer *et al.*, 2010). Thus, poststorm measurements are needed within hours to days of storms to preserve these important and time-sensitive data.

Background

Aerial photographs provide a means for quickly evaluating poststorm conditions that meets all of these needs. Visual examination of imagery provides qualitative information about coastal changes, but multiview photogrammetry (also known as structure from motion; SfM) has the potential to provide accurate quantitative information (*e.g.*, Clapuyt, Vanacker, and Van Oost, 2016; Fonstad *et al.*, 2013; Hugenholtz *et al.*, 2013; Javernick, Brasington, and Caruso, 2014; Smith, Carrivick, and Quincey, 2016). Three dimensional SfM yields a 3D reconstruction of the scene from images taken (nearly) simultaneously. Four-dimensional SfM (4D SfM) uses images made at several times (thus 4D) that include unchanged features; the additional images can strengthen the geometric reconstruction and align the images over both time and space (Warrick *et al.*, 2017). Thus, 4D SfM may be ideal for remote determination of coastal morphology before and after a storm.

Observations and assessments of coastal change on beaches and dunes has evolved over time and has included evaluations of historical photographs; maps and charts; aerial photographs; beach profiles and beach surveys using ever more accurate instruments; and various forms of remote sensing, including LIDAR, synthetic aperture radar, and multispectral imaging (Boak and Turner, 2005). Rapid measurement of beach morphology with cross-shore profiles can be performed with low-tech methods (Emery, 1961) or modern surveying equipment, but these methods require personnel on the ground, produce sparse spatial point clouds, and are time consuming for large areas (Smith, Carrivick, and Quincey, 2016). Broader surveys using ground based–remote sensing methods including cameras (*e.g.*, Holman and Stanley, 2007) or terrestrial LIDAR (*e.g.*, Hobbs *et al.*, 2010) are effective for small, selected areas (hundreds of meters), and mobile terrestrial LIDAR systems have been used for longer stretches of coast (tens of kilometers; Bitenc *et al.*, 2011; Lim *et al.*, 2013; Pietro, O'Neal, and Puleo, 2008). The current state of the art is airborne topographic–bathymetric LIDAR, which can be used for measuring coastal morphology and change at large spatial scales (hundreds of kilometers) with root-mean-squared errors (RMSE) of ~10 cm (*e.g.*, Bailly *et al.*, 2016; Brock and Purkis, 2009; Hapke *et al.*, 2010; Levoy *et al.*, 2016; Nayegandhi *et al.*,

2006; Sallenger *et al.*, 2003; Sopkin *et al.*, 2014; Stockdon, Doran, and Sallenger, 2009; Stockdon *et al.*, 2002; Wozencraft and Millar, 2005; Zhang *et al.*, 2005). Unfortunately, LIDAR is often cost prohibitive for many applications, including rapid assessment after storms.

SfM has quickly become a popular tool for measuring topography in a wide range of settings because of its accuracy, relatively low cost, and low barriers to entry (Fonstad *et al.*, 2013; Javernick, Brasington, and Caruso, 2014; Westoby *et al.*, 2012). SfM has been shown to be useful to, and embraced by, the coastal research community for mapping beaches, wetlands, and sea cliffs (Casella *et al.*, 2016; Harwin and Lucieer, 2012; James and Robson, 2012; Klemas, 2015; Mancini *et al.*, 2013; Ružić *et al.*, 2014; Schmid, Hadley, and Wijekoon, 2011; Sturdivant *et al.*, 2017; Turner, Harley, and Drummond, 2016; Warrick *et al.*, 2017). Smith, Carrivick, and Quincey (2016) provide a review of the principles and practice of SfM, and many studies have validated the use of SfM for measurement of topography in a range of environments, including coastal and riparian landscapes, hillslopes, landslides, glaciers, and coral reefs (*e.g.*, Clapuyt, Vanacker, and Van Oost, 2016; Fonstad *et al.*, 2013; Harwin and Lucieer, 2012; Hugenholtz *et al.*, 2013; Smith, Carrivick, and Quincey, 2016; Tonkin *et al.*, 2014; Westoby *et al.*, 2012; Wheaton *et al.*, 2010). Accurate SfM products can be generated using direct georeferencing of camera positions and orientations, but this approach requires real-time kinematic global navigation satellite systems (RTK-GNSS) and inertial motion units that are expensive and heavy for platforms such as drones (Chiang, Tsai, and Chu, 2012; Tsai *et al.*, 2010; Turner, Lucieer, and Wallace, 2014). However, geolocated maps can also be made with little (or no) knowledge of camera locations as long as the coordinates of at least three ground control points are visible in the scene (Smith, Carrivick, and Quincey, 2016). The RMSE of digital elevation models produced using SfM from aerial platforms (drones or manned aircraft) varies with camera focal length, lens quality, and altitude (Clapuyt, Vanacker, and Van Oost, 2016; James and Robson, 2012; Smith and Vericat, 2015), vegetation cover (Hugenholtz *et al.*, 2013), terrain steepness (Tonkin *et al.*, 2014), and number of ground control points (Clapuyt, Vanacker, and Van Oost, 2016; Tonkin and Midgley, 2016). The addition of multiple collection dates in the alignment and calibration stages results in a 4D SfM analysis that can reduce mapping errors and improve change detection, especially for photographic collections that include limited passes of the study area (Warrick *et al.*, 2017).

Objective

The objective of this paper is to evaluate the application of 4D SfM to the rapid measurement of coastal change that resulted from a large storm, Hurricane Matthew, which significantly impacted several stretches of the eastern Florida coast, as discussed in detail below. At the time of the storm (October 2016; Figure 1), the most recent published LIDAR dataset was 6 years old (JALBTCX, 2016a). (More recent prestorm LIDAR data had been collected in the spring of 2016 but remained unpublished until March 2017; JALBTCX, 2016b). After Hurricane Matthew, acquisition of poststorm LIDAR data was a high priority, but it took time: the overflight occurred 43
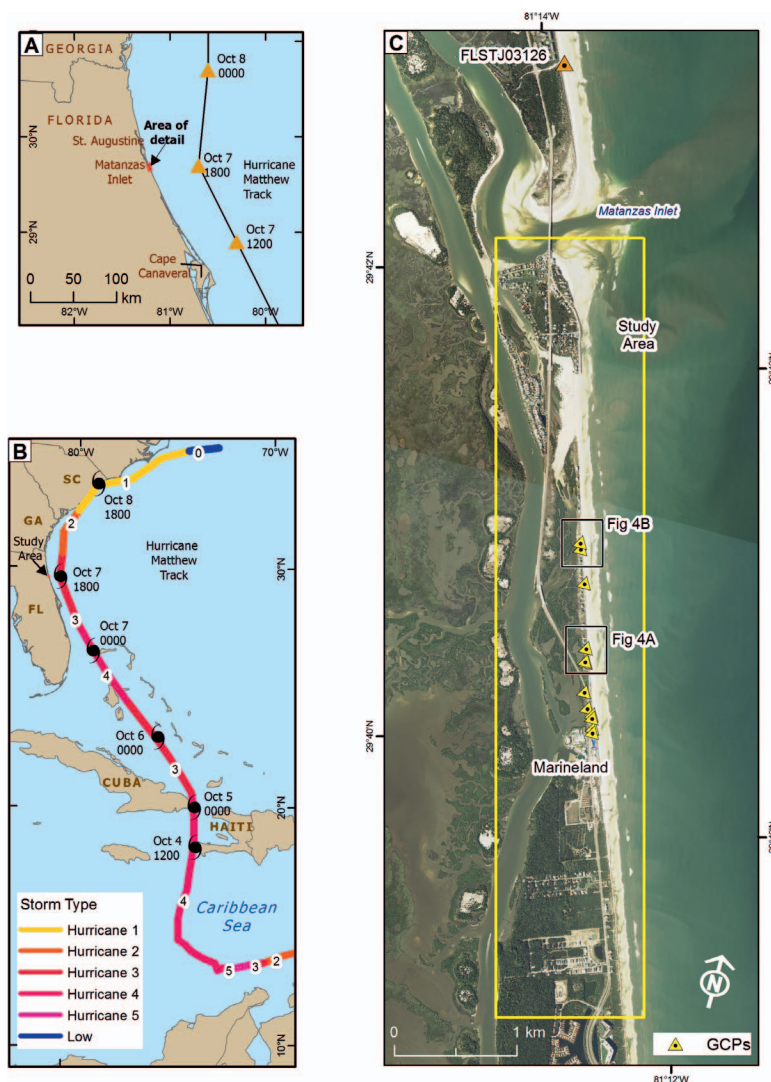
Figure 1. Study area. (a) Inset showing location of study area in NE Florida and location of Hurricane Matthew on 7 October 2016. (b) Track of Hurricane Matthew, 4–8 October 2016 colored by Saffir–Simpson hurricane wind scale. (c) Aerial photo showing the study area (yellow box), location of ground-truth survey points (yellow triangles), location of Figures 4A and 4B (black boxes), and location of USGS pressure sensor FLSTJ03126 (orange triangle).

days after the storm (20 November 2016), and the processed data were released in March 2017, 5 months after the storm (JALBTCX, 2017). In the interim, the only information on the state of the coast was from a series of oblique images acquired by the National Oceanic and Atmospheric Administration (NOAA) Remote Sensing Division on 8 October 2016, the day after the storm (NGS, 2016; NOAA, 2018a). The immediate availability of these images, along with the availability of prestorm images taken in the same area 5 months earlier (15 June 2016), enabled a pilot project to determine whether 4D SfM can provide a rapid and quantitative method for assessing coastal change after a major storm using only remotely accessed data.

This paper describes the data and photogrammetric methods used to construct both prestorm and poststorm digital elevation models (DEMs) for a portion of the eastern Florida coast using

NOAA oblique aerial photos, online data from Google Earth, and publicly available LIDAR data collected in 2010. Additionally, the differences between the prestorm and poststorm DEMs highlight patterns of coastal change, including dune erosion and overwash deposition, caused by Hurricane Matthew. Finally, a comparison of the 4D SfM DEMs with prestorm and poststorm LIDAR data demonstrates that the 4D SfM method is accurate enough to assess damage and update initial beach conditions for storm-impact models.

Study Area

Changes were examined along an ~8-km section of the east Florida coast between Marineland and Matanzas Inlet, about 25 km (15 miles) south of St. Augustine, to assess the ability for 4D SfM to produce rapid measurements of coastal change (Figure 1A). This region was selected because it was exposed to

Table 1. *Summary of LIDAR and Imagery Data.*

Dataset	Acquisition Date	Publication Date
2010 LIDAR	4 May–16 Jun 2010	16 Nov 2016
2015 pre-Matthew imagery	15 Jun 2015	Jan 2016
2016 pre-Matthew LIDAR	19 May–20 Jul 2016	15 Dec 2016
2016 post-Matthew imagery	8 Oct 2016	10 Oct 2016
2016 post-Matthew LIDAR	Nov–Dec 2016	15 Feb 2017

large waves and several meters of storm surge during Hurricane Matthew, resulting in significant morphological changes, as discussed below. The study area is represented by a sandy beach, a dune ridge with residential and commercial developments, the north–south trending Highway A1A corridor, and wetlands and open waters associated with the Matanzas River and the U.S. Intracoastal Waterway (Figure 1C).

Hurricane Matthew

Hurricane Matthew was a category 5 storm while in the Caribbean that made landfall in western Haiti on 4 October 2016, eastern Cuba on 5 October, and western Grand Bahama Island on 7 October (Figure 1B). It remained offshore as it worked up the SE coast of the United States, briefly making landfall in South Carolina on 8 October as a category 1 storm before turning east and weakening to an extratropical depression on 9 October. Sustained winds of 33–38 m/s (64–74 kts) with gusts to 47–48 m/s (91–93 kts) were measured at Cape Canaveral, Florida, as the storm passed (Stewart, 2017).

Storm tides were measured in the study area at U.S. Geological Survey (USGS) storm-tide pressure sensor FLSTJ03126 deployed on Fort Matanzas Beach, just north of Matanzas Inlet (Figure 1C), that recorded a wave-filtered storm-tide water elevation of 2.23 m North American Vertical Datum 1988 (NAVD88) on 7 October 2016 (Frantz *et al.*, 2017). For comparison, ground level at this site is 1.55 m NAVD88, and mean higher high water is approximately 0.61 ± 0.086 m NAVD88 at this location, according to the NOAA VDatum model (White *et al.*, 2016). USGS high-water mark measurements between Marineland and Matanzas inlet indicate that surge and waves drove water levels to 2.1 to 2.6 m NAVD88 m, as much as 0.8 m above local ground elevations (USGS, 2018a).

The nearest wave measurements were made at National Data Buoy Center (NDBC) buoy 41112, located ~115 km NE of the study area. These measurements indicated that waves peaked at 2100 on 7 October, with significant wave heights of 5.96 m and peak periods of 12.5 s approaching with mean incident wave directions of 122° (ndbc.noaa.gov). Waves closer to the study area may have been even larger. Simulations from the quasi-operational coupled ocean–atmosphere–wave–sediment transport (COAWST) forecast model (Warner *et al.*, 2010; USGS 2018b), which underpredicted the NDBC 41112 measurements by about 0.2 m, indicated that waves at 20-m depth offshore of Matanzas peaked at 1800 on 7 October, with significant wave heights of 7.3 m, peaks periods of 12.8 s, and mean incident wave directions of 65°. During the hurricane, significant coastal erosion, road damage, and overwash occurred between Marineland and Mantanzas, and a small breach occurred in the barrier beach, forming a new connection with the Intracoastal Waterway.

Figure 2. Detail of one of the NOAA oblique images (2106obP28254034.tif) acquired on 8 October 2016, immediately after Hurricane Matthew. See Figure 4A for location.

METHODS

Oblique aerial photographs and mulitview photogrammetery were used to reconstruct digital elevation models of the study area before and after Hurricane Matthew. This section describes the methods used, as well as LIDAR and field measurements used to evaluate the models.

Oblique Aerial Photographs

The dataset that motivated this application is a series of oblique aerial photos taken on 8 October 2016, the day after Hurricane Matthew passed the Florida coast. The images were acquired by the NOAA Remote Sensing Division from altitudes of about 760 to 1500 m (2500 to 5000 feet) using a Trimble Digital Sensor System (NGS, 2016) at a look angle of 37.5° from vertical. The images had pixel dimensions of 7212×5408, and the ground sample distance (GSD) for each pixel was approximately 0.35 to 0.50 m (NOAA 2018b). Images along each flight line overlapped by 60–70%. The images were made publicly available by NOAA and downloaded on 10 October 2016, only 3 days after the storm (Table 1). An inset from one of the images looking shoreward (roughly west) shows damage to the roadway of old route A1A (in foreground at top of beach) and overwash deposits landward of the houses (Figure 2).

Images of the study area were also taken by NOAA on 15 June 2015 (Table 1), which is slightly greater than 1 year before Hurricane Matthew, and these photos were used here to represent the prestorm conditions. These photos are available through NOAA's Coastal Imagery Viewer (NOAA, 2018c).

4D Structure-from-Motion Point Clouds

Multiview stereo photogrammetry (structure from motion; SfM) was used to make topographic point clouds of the study area before and after Hurricane Matthew. Images from both 2015 and 2016 were aligned together using Agisoft Photoscan v. 1.2.x using a technique termed 4D SfM (Warrick *et al.*, 2017). This technique develops tie points across both image sets simultaneously during the alignment and subsequent optimization of the lens calibration and camera locations and view directions. Photoscan was used because it facilitates grouping images by time and because it has demonstrated excellent performance in some software comparisons (Turner, Lucieer, and Wallace, 2014). Tie points are locations identified with
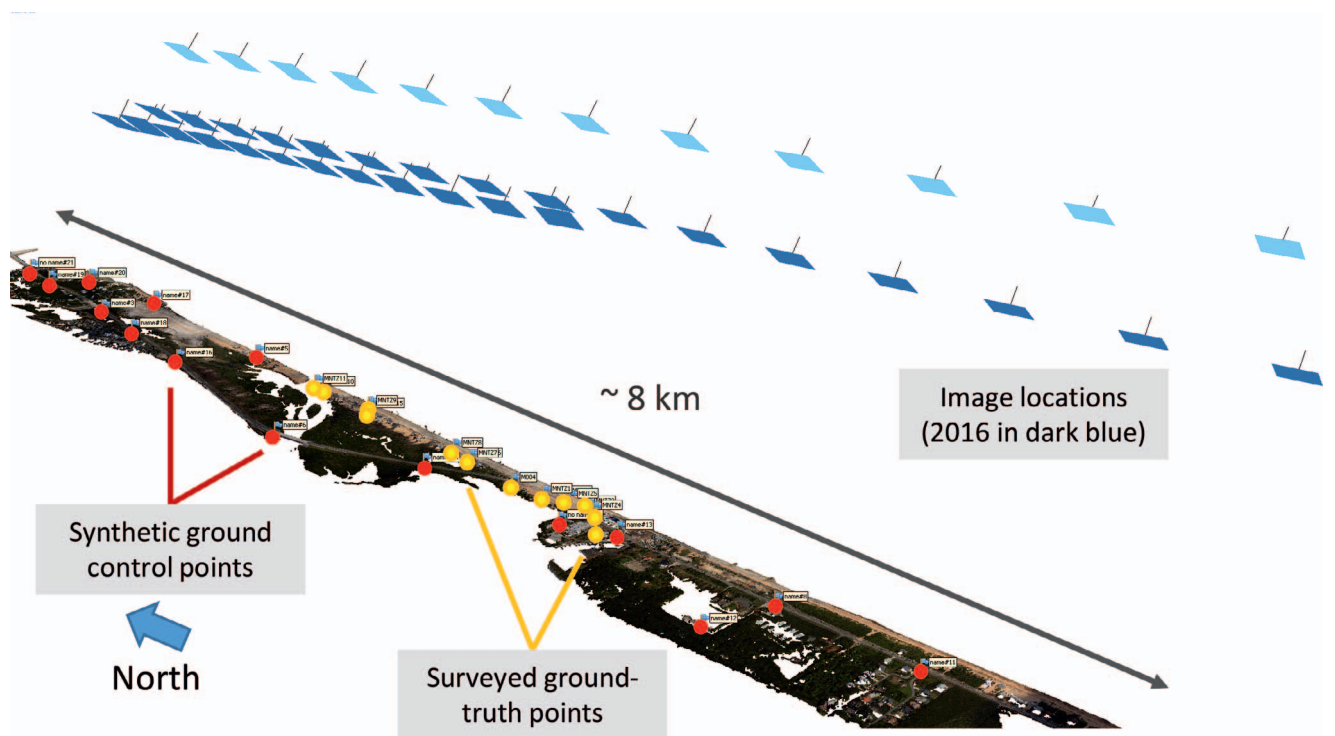
Figure 3. Illustration of the structure-from-motion (SfM) reconstruction. This is an oblique 3D view of the point cloud (>30 million points) of the reconstructed landscape, looking NE (offshore). The blue flags with red dots indicate locations of the synthetic ground control points (SGCPs). The ground-truth points are indicated with blue flags and yellow dots. The inferred camera locations are indicated by light blue (2015) and dark blue (2016) image planes.

computer vision algorithms as representing the same feature in two or more images. The advantage of 4D SfM is that the features within the study area that are unchanged between the photo collection dates provide extra candidate tie points, thus strengthening the geometrical reconstruction.

Alignment

The camera alignment process involved several steps. All of the available images (13 from 2015 and 29 from 2016; Figure 3) were imported into two camera groups. Masks were created to outline and remove portions of the images that contained water or were above the horizon. The masked images from both years were aligned together, allowing the software to infer separate lens calibration coefficients for each flight. Following the initial alignment, an iterative procedure was used to identify and remove tie points with weak geometry and readjust the camera alignment (Breithaupt *et al.*, 2004; Matthews, Noble, and Breithaupt, 2016; Noble, *personal communication*, 2016; Thoeni *et al.*, 2014; Warrick *et al.*, 2017). After this optimization, the remaining sparse point cloud contained 71,796 tie points.

Synthetic Ground Control Points

Ground control points (GCPs) are required to accurately georeference SfM point clouds, but the NOAA oblique photos were collected independently of any ground-truth data. James *et al.* (2006) have shown that LIDAR-derived GCPs were almost as effective as surveyed GCPs for improving the

accuracy of SfM DEMS. The most recent LIDAR data that were publicly available at the time of the storm were from a 2010 survey published on the NOAA Digital Coast website in 2016 (NOAA, 2018d; JALBTCX, 2016a). These data were part of a coastal survey extending from Cape Canaveral, Florida, to Cape Lookout, North Carolina, from the waterline inland about 500 m and were used to create the synthetic ground control points used in SfM reconstruction.

A set of synthetic ground control points (SGCPs) was developed using a combination of Google Earth imagery for horizontal coordinates and the 2010 LIDAR dataset (JALBTCX 2016a) for elevations. Ideally, GCPs are placed in flat sections of the landscape, are precisely located, and are readily identifiable in multiple aerial images. Painted road strips, manhole covers, and seams on pavement or flat roofs are suitable targets. While LIDAR data provide precise positioning, it is difficult to use LIDAR output (elevation and intensity) to find flat-lying features that can be unambiguously identified in aerial images. A novel combination of Google Earth images (to identify visible features) and LIDAR positioning (to better constrain vertical elevations) was developed. This was predicated on the ease of colocating features such as road stripes in both the oblique aerial photos and Google Earth and the reported horizontal accuracy of Google Earth (RMSE ranging from 0.67 to 5 m; Goudarzi and Landry, 2017; Mohammed, Ghazi, and Mustafa, 2013; Paredes-Henández *et al.*, 2013; Wang *et al.*, 2017). This level of accuracy was judged to be

better than that of horizontal positions extracted from LIDAR and the oblique imagery. Google Earth was not used for vertical positions, owing to the larger errors in Google Earth elevations reported by Wang *et al.* (2017).

The locations of useful SGCPs were constrained by the geography of the study area, which included beaches, wetlands, and the Matanzas River. Within these constraints, an attempt was made to distribute SGCPs fairly uniformly around the study area, with emphasis on cross-shore distributions to help constrain the geometry along that axis. After some assessment of the NOAA and Google Earth imagery and the LIDAR data, 16 points were identified (Figure 3) and assigned horizontal coordinates from Google Earth positions and elevations from the LIDAR data at the same location. Horizontal coordinates for this project were projected to Universal Transverse Mercator (UTM) Northing and Easting (meters, zone 17 North) in the North American Datum 1983 (NAD83) reference frame (Geoid12a). Vertical coordinates were meters referenced to NAVD88.

The coordinates of the SGCPs were imported into Photoscan and manually located on each of the images in which they appeared. These points were assigned marker accuracies of 2 m (horizontal; Mohammed, Ghazi, and Mustafa 2013) and 0.1 m (vertical; JALBTCX, 2016a) in Photoscan. Camera location accuracy was set at 10 m (the default); tie-point accuracy was set at 0.1 pix (following guidance of Noble, *personal communication*, 2016). The accuracy assigned in Photoscan to various inputs (camera locations, tie points, GCP locations) determined the weights assigned in the overall optimization of the reconstruction. After placing the SGCPs in the project, the geometry and lens calibration coefficients were optimized a final time to account for the additional constraint of the SGCPs (Figure 3). The standard error of unit weight reported by Photoscan after optimization was 1.16; a value of 1.0 indicates that the weighted errors are perfectly equally distributed among the various inputs.

Photogrammetry Products: Point Clouds, DEMs, Orthomosaics, and Difference Maps

Two geolocated point clouds were constructed independently using the aligned images from pre- and post-Matthew using Photoscan with the high density setting and the moderate depth filtering algorithm. This resulted in prestorm and poststorm point clouds with 22.6 million and 33.2 million data points, respectively. The point clouds were unclassified but included red–green–blue (RGB) colors for each point interpolated by Photoscan from the original photographs.

Digital elevation models (DEMs) were interpolated from the dense point clouds using inverse-distance weighting in Photoscan and exported at 0.5-m resolution. No manual editing of the point clouds was performed prior to interpolation. The term DEM is used here for both the SfM and LIDAR products (discussed below), recognizing that the two technologies are mapping different surfaces. Orthomosaics were also constructed in Photoscan using the aligned images and the DEMs and exported at 0.25-m resolution. The DEMs were differenced in Global Mapper (v.17.2) (post- minus pre-Matthew) to quantify changes between 15 June 2015 and 8 October 2016.

Topo–bathy LIDAR Products: Point Clouds and DEMs

Topographic–bathymetric (topo–bathy) LIDAR data were acquired in the study area before and after Hurricane Matthew (in June 2016 and November 2016, respectively; Table 1), but these were not available for analysis in the immediate aftermath of the storm. However, they were released months later (December 2016 and February 2017, respectively; Table 1) and were used retrospectively to assess the quality of the SfM reconstruction. Both datasets were obtained with the U.S. Army Corps of Engineers (USACE) Coastal Zone Mapping and Imaging LIDAR (CZMIL) system. CZMIL integrates a topo–bathy LIDAR sensor with a digital camera and a hyperspectral imager on a single remote sensing platform. Topo–bathy LIDAR data were collected before Hurricane Matthew by the USACE on 24 June 2016 and published on 15 December 2016 (JALBTCX, 2016b; Table 1). Similar data were collected after Hurricane Matthew (JALBTCX, 2017) with flights over the study area on 20 November 2016. Several field crews from the USGS used survey equipment to provide ground-truth measurements along the flight lines, and the LIDAR data were published on 15 February 2017 (Table 1).

Topo–bathy point clouds from the 2016 pre- and post-Matthew surveys were classified as either 1 = Unclassified, 2 = Ground, or 29 = Bathymetry. The data were distributed in compressed LAS format as LAZ files (ASPRS, 2013; Isenburg, 2013). LAZ files were imported to Global Mapper for an area covering approximately 8 km of coast south of Matanzas Inlet and displayed as point clouds. Only the ground (bare earth) points (point class 2) were used for this analysis; they accounted for 15–20% of the overall points in each tile. One-meter DEMs were created from the pre- and post-Matthew ground point clouds and exported as 32-bit floating point GeoTIFF files.

The two LIDAR DEMs were differenced in ArcGIS (v. 10.2) to measure change between June and October 2016. The stated vertical accuracy of the USACE LIDAR data is 0.196 m at 95% confidence interval. Although the two LIDAR surveys were collected by the same organization using the same sensor, vertical differences existed in areas where there should have been no changes. These areas were used to calculate and remove a 0.17-m bias between the pre- and post-Matthew LIDAR point clouds, as follows. The road centerline of new state route A1A was obtained from the Florida Department of Transportation, and a 1-m buffer was added to create a 2-m wide strip along the road centerline. The mean change value of this strip was 17 cm, with the post-Matthew LIDAR data higher than the pre-Matthew survey. The post-Matthew DEM was adjusted by subtracting 0.17 m, and the difference map was recalculated. This approach has been applied elsewhere when there are multiple colocated LIDAR data sets (Thompson *et al.*, 2017).

Ground-Truth Survey Points

The USGS deployed a survey crew to the Matanzas study area to collect ground-truth measurements 6 days after the storm (13 and 14 October 2016). The team identified 12 points on features that were likely to be visible in the aerial photos and that did not appear to have moved since the storm (Supplemental Material). The points included corners of

asphalt and concrete slabs, the ends of exposed water pipes, the end of a wall, a dune scarp, a nearly buried fire hydrant, and the trunk of a downed palm tree. The points were located by setting up a GNSS surveying system (Ashtech GNSS antenna and Ashtech Proflex 800 receiver) on a tripod over the feature and collecting satellite observations for 5 minutes. These data were postprocessed to provide positions with horizontal precision of ~1.5 cm and vertical precision of ~3.5 cm, based on the maximum standard deviations in the recorded time series, instrument precision, and distance (<1 km) from the base station to the surveyed point.

The ground-truth features were identified in the oblique aerial images, and the photogrammetry software was used to compare their surveyed locations with the locations determined using the 4D SfM reconstruction. In some cases, it was difficult to determine the exact location of the ground-truth feature in the oblique image, either because the feature was not fully resolved, the look angle hid part of the feature, or because the location of the feature was ambiguous in the field notes and photographs. Vertical positioning was considered compromised when the feature was prominent relative to its immediate surroundings and when small errors in the horizontal position could have led to substantial vertical differences. Horizontal positioning was considered compromised if the feature was indistinct or difficult to locate precisely in the oblique photos. Despite the difficulty in precisely locating these points in the oblique photos, they provide some information about the accuracy of the SfM reconstruction on the beach.

RESULTS

The methods described above generated orthomosaics and DEMs that were used to make difference maps. This section describes the changes observed in the orthomosaics, DEMS, and difference maps and compares the DEMs and the difference maps with LIDAR data and ground-truth points.

4D SfM Orthomosaics and DEMs

Results from the 4D SfM process include orthomosaics, DEMs that were used to make difference maps, and cross-shore profiles at representative cross-sections devoid of vegetation or structures. Comparison of orthomosaics and DEMs before and after Hurricane Matthew reveal distinct changes in coastal features. Examples from two sites are shown in Figure 4. The panels on the left show data from a southern site with significant beach erosion and overwash. The panels on the right show data from a region a few hundred meters farther north, where a breach in the barrier beach formed during the storm.

The pre-Matthew orthomosaic at the southern site (Figure 4A) shows a stretch of coast with houses built on the dune crest landward of old route A1A. New route A1A curves inland behind a wetland west of the houses (upper left corner of the images). The post-Matthew orthomosaic (Figure 4C) shows destruction of old route A1A, modification of the dune line, and formation of distinctive orange sand overwash deposits between the houses. Orthomosaics at the northern site show a thin stretch of barrier beach before Hurricane Matthew (Figure 4B). After Hurricane Matthew, the orthomosaic shows that a breach has formed, and the barrier has migrated inland

through erosion of the shoreface and overwash deposition in the back-barrier river channel (Figure 4D).

DEMs produced by 4D SfM (Figure 4E–H) were differenced to quantify changes for these sites (Figure 4I–J). The difference maps were shaded to indicate regions of erosion (red) and deposition (blue). Changes less than ±0.5 m are unshaded. These difference maps showed erosion at the dune crest and along old route A1A and smaller amounts of erosion on the beach face (Figure 4I). Deposition in the developed portion of the coast occurred in overwash lobes that formed between houses. Erosion was more widespread at the northern section where a new breach formed, but overwash resulted in deposition in the back-barrier waterway (Figure 4J).

The vertical changes are shown more clearly in profiles across the beach extracted from the SfM DEMs at two locations (profiles P9 and P6 in Figure 4). At the northern profile (P6), the dune crest was eroded by as much as ~2 m, and an overwash lobe was deposited that was nearly ~1 m thick (Figure 5A). At the southern profile (P9) the beachface was lowered by ~0.3 m, the dune crest reduced by ~1.5 m, and the overwash lobe was ~1.2 m thick as it extended into the small pond west of the barrier (Figure 5B).

Comparison with LIDAR DEMs

The vertical uncertainty associated with the SfM reconstruction can be assessed roughly by comparison with the LIDAR data. A global assessment over the entire DEM is not useful because the LIDAR surfaces do not contain structures or vegetation, whereas the SfM surfaces contain both. Additionally, the DEMs are not contemporaneous: the pre-Matthew imagery and LIDAR are nearly a year apart, and the post-Matthew imagery and LIDAR are 6 weeks apart. Therefore, some of the measured differences are real changes related to natural processes and human activity. That noted, the difference maps using SfM and LIDAR show spatial patterns of deposition and erosion that agree well over most of the study area (Figure 6). Both maps indicate erosion of the dune crest along nearly the entire reach, usually with deposition immediately landward. Farther west, in the vegetated wetlands, the patterns of erosion and deposition are irregular and probably mostly artifacts of vegetation and/or water levels. In the northern part of the study area (in the region of profiles P1–P3), the LIDAR difference map shows deposition on the upper portion of beach and broad regions of erosion west of the dune crest. However, an examination of imagery available from Google Maps (accessed 21 December 2017) revealed that significant human modification occurred in this region, involving removal of sand from the overwash deposits and construction of a new, artificial dune seaward of the preexisting dune crest. These changes occurred after the SfM imagery was collected but were in progress during the LIDAR flight.

More comparisons can be made along the profiles shown in Figure 6. Profiles P6 and P9 are the same as Figure 5 but now include pre-Matthew (green) and post-Matthew (blue) profiles from the LIDAR data (darker thin lines). The other cross-barrier profiles were extracted at irregular but representative locations with bare sand or sparse vegetation. Profiles P4 and P7 are plotted along with P4 and P9 in Figure 6. There is good qualitative agreement between SfM and LIDAR elevations in
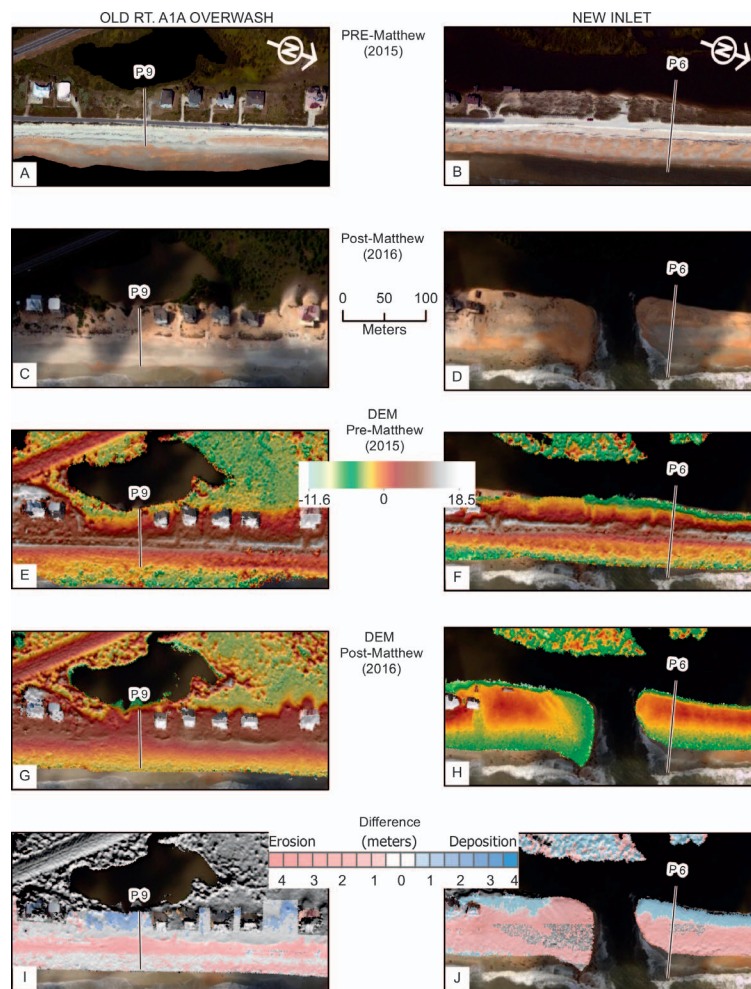
Figure 4. Orthomosaics at two locations in the study area (Figure 1) constructed from pre-Matthew (A, B) and post-Matthew (C, D) oblique images using 4D SfM, with corresponding DEMs (E, F and G, H). Difference maps calculated from the DEMs (I, J) show regions of erosion (red) and deposition (blue); the white region indicating no significant difference extends from −0.5 to +0.5 m. Dark regions in the DEMs and difference maps are regions with no data. P9 and P6 indicate locations of elevation profiles that are presented in Figure 5.

all of the profiles except profiles P4 and P6, where there are differences between the poststorm LIDAR and SfM of 0.5 m (P4) and 1.1 m (P6). In profile P4, the post-Matthew LIDAR profile is higher on the upper beach. Google Maps images indicate that a roadbed was constructed here after the date of the SfM imagery. Profile P6 was located at the northern edge of the new breach, another place where rapid poststorm changes occurred as the inlet evolved naturally and construction crews worked to close it. The root-mean-square difference (RMSD) computed for the eight pairs (SfM *vs.* LIDAR) of profiles ranged from 0 to 0.75 m, with a mean of 0.18 m (Figure 6). The mean RMSD for all 10 of the pre-Matthew profiles SfM/LIDAR pairs was 0.18 m, and for the post-Matthew profile pairs the mean RMSD was 0.20 m. The real changes that occurred between the SfM and LIDAR acquisition dates are included in this calculation, so 0.2 m is a realistic estimate of the vertical accuracy of the SfM elevations on bare sand along the profiles.

Elevations for all five datasets (2010 LIDAR, 2016 pre-Matthew LIDAR, 2016 post-Matthew LIDAR, 2015 pre-Matthew SfM, and 2016 post-Matthew SfM) were compared along a swath 60 m long and 2 m wide down the middle of the paved highway near the intersection of route A1A with old A1A, a section that appeared to be devoid of cars or overwash in all five datasets. The 2016 pre-Matthew LIDAR elevations were used as a reference and subtracted from the other datasets along the profile. The 2010 and 2016 post-Matthew LIDAR datasets showed mean differences (RMSD) of −0.07 (0.07) m and −0.02 (0.02) m, respectively. (Note that the 2016 post-Matthew LIDAR was previously adjusted 0.17 m to match the pre-Matthew LIDAR along a slightly different portion of the road.) The pre- and post-Matthew SfM profiles showed differences of −0.18 (0.20) m and −0.25 (0.26) m, respectively. These were slightly larger differences than occurred along the cross-shore profiles. The mean difference (RMSD) between the two SfM road profiles was 0.07 (0.10) m. These suggest that, in
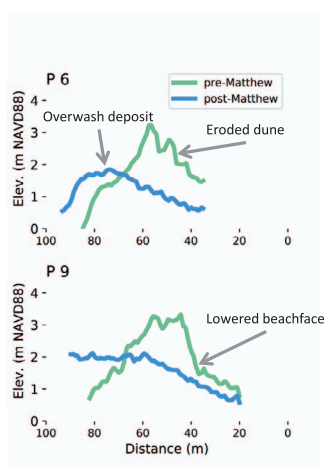
Figure 5. Profiles extracted from the SfM DEMs across the beach at two locations indicated in Figure 1C and Figure 4. Distance is measured from the approximate water line in pre-Matthew LIDAR DEMs.

this region, the SfM reconstructions were biased low by −0.18 to −0.25 m relative to the pre-Matthew LIDAR but matched each other within 0.10 m.

Comparison with Ground-Truth Survey Points

Twelve ground-truth features were surveyed, but one had clearly moved and was not used. All of the 11 reconstructed locations in the 4D SfM DEMs fell within 1.27 m (horizontal) and 1.4 m (vertical) of the ground-truth features identified by the survey crew (Supplemental Material). The mean horizontal difference (bias) was 0.79 m, with a range of 0.36 to 1.27 m and RMSD of 0.83 m. The vertical bias was 0.48 m, with a range of −0.33 to 1.4 m and RMSD of 0.48 m. Some features were likely to be more reliable than others. For example, it was difficult to determine the exact point where the survey instrument was located in an image of the eroded dune scarp. Similarly, small changes in positioning the survey point in images of water pipes or a stone wall resulted in large vertical changes. Removing from the comparison features with questionable horizontal positioning does not make much difference, but when features with questionable vertical positioning are eliminated, the vertical bias in the five remaining points decreases to −0.09 m, with an RMSD of 0.12 m and a range of −0.18 to 0.02 m. These results are consistent with the LIDAR comparisons in the previous section and indicate that the SfM elevations are accurate to within ∼0.2–0.25 m.

DISCUSSION

The rapid collection of oblique photographs by the NOAA Remote Sensing Division after Hurricane Matthew, combined with prestorm imagery, provided adequate imagery to develop 4D SfM topographic models that characterized changes in coastal morphology resulting from the storms. Here the utility of these data products is evaluated, considering their accuracy and timeliness, especially with respect to LIDAR collections.

Accuracy and Precision

A crucial question is whether the SfM reconstructions using the techniques here are accurate enough for a rapid assessment of coastal change. LIDAR data are the standard for comparison. There are a number of important differences between DEMs created with SfM and LIDAR. LIDAR point clouds are classified and can usually provide bare-earth surfaces. Most SfM point clouds are initially unclassified and, while they have colors that help identify features on the landscape, the DEM surfaces include vegetation, structures, vehicles, and other features that are not included in the LIDAR ground class. Commonly, LIDAR data have been quality checked and have been compiled to meet horizontal and vertical accuracies of 1 m and 19.6 cm, respectively, at the 95% confidence limits (JALBTCX, 2016a,b). However, in this case, a 17-cm discrepancy was found between the two LIDAR data sets that would have biased difference maps had it not been found and removed. Standardized quality assurance procedures for 4D SfM have not been established, but the horizontal accuracy of the SfM reconstructions showed a mean bias of 0.79 m with a maximum error of 1.27 m, a consequence of referencing the SGCPs to Google Earth. The horizontal resolution of the SfM orthomosaics (0.1 m) and DEMs (0.5 m) allows precise comparisons between pre- and post-Matthew maps. The estimates of vertical uncertainties in the SfM DEMs were ∼0.25 m, as judged by both comparison with LIDAR and independent ground-truth points. The 4D SfM methodology minimized biases between the two SfM DEMs, and the difference maps appear to be biased by less than 0.07 m. Additionally, the spatial distribution of the changes is qualitatively similar to those inferred from pre- and post-Matthew LIDAR maps, with most differences appearing either on the lower shoreface, near the new breach, or on the wetlands landward of the barrier (vicinity of profiles P1–P5; Figure 6). All of this evidence suggests that sufficient precision exists in the difference maps to identify the observed changes of a meter or more.

Artifacts in the LIDAR data are fairly well understood and include biases across flight lines, scattered returns associated with vegetation and power lines, and lost returns from light-absorbing surfaces including water. Artifacts in the SfM data arise for other reasons, including global biases associated with error in the GCP locations and regional distortions caused by misalignment of the camera locations and imperfections in the inferred camera lens model. In addition, the SfM reconstructions contain artifacts caused by shadows and moving objects, such as water and wind-blown vegetation. However, the additional information provided by the orthomosaics greatly enhances the interpretive value of the SfM DEMs. The coregistration of the SfM elevation and underlying imagery allows for very clear characterization of coastal changes and their impacts to infrastructure and ecosystems. Thus, SfM results can be used to describe changes in features such as houses, roads, and wetlands (*e.g.*, Figure 4), which would support simultaneous estimation of elevation change and economic loss due to storm damage (Liu *et al.*, 2014). These sorts of data are needed to develop and test improved risk reduction methods that go beyond assessing coastal hazards (*e.g.*, van Verseveld *et al.*, 2015).
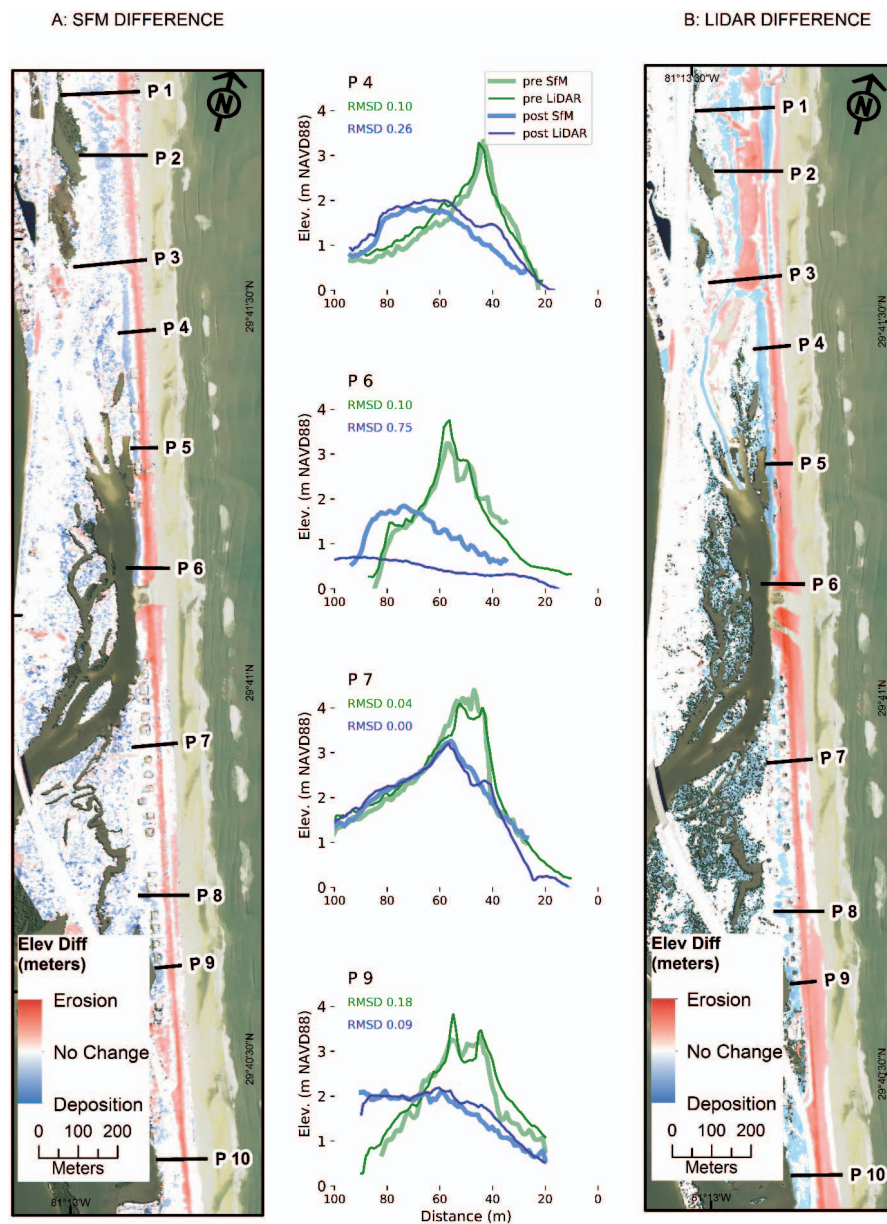
Figure 6. Difference maps and profiles. Left panel: difference map from 4D SfM (pre-Matthew, 15 June 2015; post-Matthew, 8 October 2016). Right panel: difference map from airborne LIDAR (pre-Matthew, 24 June 2016; post-Matthew, 20 November 2016). The color scale is the same in both difference maps; the white region indicating no significant difference extends from −0.5 to +0.5 m. Middle panels: profiles P4, P6, P7, and P9 from SfM and LIDAR at selected cross-sections (green, pre-Matthew; blue, post-Matthew; thick, SfM; thin, LIDAR); and RMSD between the pre-Matthew (green) and post-Matthew (blue) SfM and LIDAR profiles.

The coastal zone LIDAR system includes a blue-green LIDAR that acquires bathymetric data in the nearshore region (Feygels *et al.*, 2013; Tuell, Barbor, and Wozencraft, 2010). Although the working depth varies with water clarity, these data are very useful for assessing changes in coastal morphology. At present, estimates of bathymetry cannot be extracted using SfM from coastal images with waves.

Many of the differences between SfM and LIDAR maps were real changes resulting primarily from human recovery efforts,

reflecting the timing of data collection. Where beach modifications occurred between the dates when LIDAR and SfM were acquired, the differences between the two data sets were over 1 m, exceeding the 0.25 m RMSD estimate. In these cases, the SfM elevations are more accurate estimates of changes associated with Hurricane Matthew. Applications of LIDAR elevation data to test model accuracy often identify areas of mismatch between modeled and observed elevation changes that are blamed on timing of data acquisition (Lindemer *et al.*,

2010; McCall *et al.*, 2010; Sherwood *et al.*, 2014). At remote locations, human interference cannot be blamed for mismatches, but continued coastal evolution may occur, particularly if an area has been breached. Rapid observations can help to avoid the convolution of model errors, observation errors, and actual landscape evolution.

Spatial Coverage

Point densities varied for both methods, and gaps in coverage occurred for different reasons. The LIDAR data had variable point densities ranging from ~10 to 40 points/m^2, dropping to zero in regions where the bare-earth algorithm had removed structures. The SfM point cloud was more uniform, ranging from about 10 to 17 points/m^2, dropping to zero in water and behind tall objects (including houses) where the look angle was obscured.

LIDAR missions typically cover large regions of the coast. For example, the post-Matthew flight extended from Florida to North Carolina, and post-Sandy flights extended from Long Island to Maryland (NOAA, 2018e). SfM maps are usually made for smaller survey areas, but the NOAA oblique images used here were part of a much longer mission, extending from South Carolina to south Florida, with approximately five images per kilometer. A 4D SfM project for 100 km of coastline would involve ~1000 images.

Timeliness

The objective of this pilot application was to evaluate 4D SfM as a rapid assessment tool, which includes rapid data acquisition and can include the rapid processing and dissemination of the results. Thus, it is also important to discuss the timing of the analyses and results. User-friendly software packages with sophisticated algorithms (*e.g.*, Agisoft Photoscan, Pix4D, Correlator3D) are commercially available and can be used effectively with only a moderate amount of training. In this case, most of the processing effort involved identifying the SGCPs and masking the images to remove water. This work required about 8 person-hours. After the workflow was established and the SGCPs were established, the actual photogrammetric processing took about 4 person-hours and overnight processing on a high-end workstation. Thus, it would be reasonable for a small team to provide difference maps for small regions within 48 hours of receipt of the images. This turnaround time could be reduced with more resources, especially if automatic water-masking algorithms were used and if SGCPs were preselected for vulnerable regions before or during storms. In contrast, LIDAR data are routinely processed by contract specialists with dedicated software and multistep workflows. These procedures produce a consistent and reliable product covering a much larger region, but processing times are usually weeks to months, rather than hours.

Both approaches require well-timed datasets. In the past, coastal LIDAR mapping missions have been flown on an irregular schedule, and while parts of eastern Florida have been mapped six times between 2004 and June 2017, other portions of the U.S. coast have never been mapped with modern topo–bathy LIDAR (A. Fredericks, U.S. Geological Survey, *personal communication*, 2017; Wozencraft, 2017). Unless resources are dedicated to mapping after a specific event, the interval between LIDAR maps is likely to range from 1 to 5 years.

The 4D SfM method depends on good quality images before and after the event of interest. Imagery is collected more frequently than LIDAR: NOAA acquires imagery after most damaging hurricanes, and other organizations, including state emergency management agencies and the USGS, often arrange for aerial photo collection after major coastal events. Most of the east and Gulf coasts of the U.S. have been imaged recently, but not all imagery is ideally suited for SfM processing. For example, the images acquired during the 2017 hurricane season were distributed in an orthometric format with minimal overlap, making them unsuitable for SfM analysis. Ideally, photos should overlap by about 60% and would not be processed in a way that degrades the ability for pixel mapping. Acceptable images may be acquired from other light planes with hand-held cameras if static camera settings and photographic overlap requirements are implemented, which means that local Civil Air Patrol wings or contractors can help assess poststorm conditions and topographic change. Given the lower cost for both photo acquisition and SfM processing compared with LIDAR data, it is anticipated that aerial images will be more readily available along many coastal reaches, making the 4D SfM a practical alternative for future change assessments.

SfM projects involving ~1000 images (~100 km of coastline) can be easily processed overnight on a workstation with a high-end graphics card with a graphics processing unit (GPU) and a moderate amount of memory (~16–32 GB). High-performance computing resources with tens of GPUs and large shared memory can process projects with tens of thousands of images. With planning, sufficient trained assistance, and adequate computer resources, it would be technically feasible to scale the SfM analysis to incorporate the larger domains usually mapped with LIDAR. It is also possible to incorporate a wider source of images, as demonstrated by the use of crowd-sourced images (*e.g.*, Frahm *et al.*, 2013), and leverage the growing number of cloud resources to render large-scale SfM processing.

CONCLUSIONS

Digital elevation models (DEMs) of coastal regions produced from aerial photos can be used to rapidly assess storm impacts. NOAA oblique aerial imagery, combined with a photogrammetric technique that incorporated imagery from multiple viewpoints at several times (known as four-dimensional structure-from-motion; 4D SfM) and synthetic ground control points derived from publicly available sources, produced DEMs that agreed both qualitatively and quantitatively with DEMs generated from LIDAR data. Vertical RMS differences between LIDAR and SfM were 0.20–0.25 m, which are sufficiently precise to resolve beach changes caused by major storms, which are often more than 1 m. The main benefit of using these SfM methods is timeliness. Oblique aerial imagery can be acquired and made available within hours to days after significant storms such as Hurricane Matthew. Timely acquisition can avoid confusing observation errors with actual beach changes that occur after, and are unrelated to, a major storm event. Accuracy improvement from timely observations was shown to be as much as 1 m where beach modification had begun after the storm passed but prior to LIDAR acquisition. This pilot

application of the 4D SfM method demonstrates that photogrammetric analysis of a multiple-kilometer coastal region can be performed by a small team with modest computer resources in 48 hours from receipt of the images, producing orthomosaics and digital elevation models with an RMS error of ~0.25 m. Larger regions or faster turnaround could be processed with more computer resources, multiple teams, and/or prior planning. The timeliness of these quantitative products makes them valuable for rapid assessment of coastal change.

ACKNOWLEDGMENTS

LITERATURE CITED

Angnuureng, D.B.; Almar, R.; Senechal, N.; Castelle, B.; Addo, K.A.; Marieu, V., and Ranasinghe, R., 2017. Shoreline resilience to individual storms and storm clusters on a meso-macrotidal barred beach. *Geomorphology,* 290, 265–276. https://doi.org/10.1016/j.geomorph.2017.04.007

ASPRS (American Society for Photogrammetry & Remote Sensing), 2013. *LAS Specification Version 1.4–R13*. American Society for Photogrammetry & Remote Sensing. https://www.asprs.org/committee-general/laser-las-file-format-exchange-activities.html

Bailly, J.-S.; Montes-Hugo, M.; Pastol, Y., and Baghdadi, N., 2016. Chapter 5—Lidar measurements and applications in coastal and continental waters. *In:* Baghdadi, N. and Zribi, M. (eds.), *Land Surface Remote Sensing in Urban and Coastal Areas*. Amsterdam: Elsevier, pp. 185–229.

Barnard, P.L.; Hoover, D.; Hubbard, D.M.; Snyder, A.; Ludka, B.C.; Allan, J.; Kaminsky, G.M.; Ruggiero, P.; Gallien, T.W.; Gabel, L.; McCandless, D.; Weiner, H.M.; Cohn, N.; Anderson, D.L., and Serafin, K.A., 2017. Extreme oceanographic forcing and coastal response due to the 2015–2016 El Niño. *Nature Communications,* 8, 14365.

Barnard, P.L.; van Ormondt, M.; Erikson, L.H.; Eshleman, J.; Hapke, C.; Ruggiero, P.; Adams, P.N., and Foxgrover, A.C., 2014. Development of the coastal storm modeling system (CoSMoS) for predicting the impact of storms on high-energy, active-margin coasts. *Natural Hazards*, 74(2), 1095–1125.

Bitenc, M.; Lindenbergh, R.; Khoshelham, K., and Van Waarden, A.P., 2011. Evaluation of a LIDAR land-based mobile mapping system for monitoring sandy coasts. *Remote Sensing*, 3(7), 1472–1491.

Boak, E.H. and Turner, I.L., 2005. Shoreline definition and detection: A review. *Journal of Coastal Research*, 21(4), 688–703.

Breithaupt, B.H.; Neffra A.; Matthews, N.A., and Noble, T.A., 2004. An integrated approach to three-dimensional data collection at dinosaur tracksites in the Rocky Mountain west. *Ichnos*, 11(1–2), 11–26. doi:10.1080/10420940490442296

Brock, J.C. and Purkis, S.J., 2009. The emerging role of lidar remote sensing in coastal research and resource management. *In:* Brock, J.C. and Purkis, S.J. (eds.), *Coastal Applications of Airborne Lidar*. *Journal of Coastal Research*, Special Issue No. 53, pp. 1–5.

Brock, J.C.; Wright, C.W.; Sallenger, A.H.; Krabill, W.B., and Swift, R.N., 2002. Basis and methods of NASA airborne topographic mapper lidar surveys for coastal studies. *Journal of Coastal Research*, 18(1), 1–13.

Casella, E.; Rovere, A.; Pedroncini, A.; Stark, C.P.; Casella, M.; Ferrari, M., and Firpo, M., 2016. Drones as tools for monitoring beach topography changes in the Ligurian Sea (NW Mediterranean). *Geo-Marine Letters*, 36, 151–163.

Chiang, K.-W.; Tsai, M.-L., and Chu, C.-H., 2012. The development of an UAV borne direct georeferenced photogrammetric platform for ground control point free applications. *Sensors,* 12(7), 9161–9180.

Clapuyt, F.; Vanacker, V., and Van Oost, K., 2016. Reproducibility of UAV-based earth topography reconstructions based on Structure-from-Motion algorithms. *Geomorphology*, 260, 4–15.

Emery, K.O., 1961. A simple method of measuring beach profiles. *Limnology and Oceanography*, 6(1), 90–93.

Feygels, V.I.; Park, J.Y.; Wozencraft, J.; Aitken, J.; Macon, C.; Mathur, A.; Payment, A., and Vinod Ramnath, V., 2013. CZMIL (coastal zone mapping and imaging lidar): From first flights to first mission through system validation, *Proceedings of SPIE Defense, Security, and Sensing–Ocean Sensing and Monitoring V* (Baltimore, Maryland), 87240A. doi: 10.1117/12.2017935

Fonstad, M.A.; Dietrich, J.T.; Courville, B.C.; Jensen, J.L., and Carbonneau, P.E., 2013. Topographic structure from motion: A new development in photogrammetric measurement. *Earth Surface Processes and Landforms*, 38, 421–430.

Frahm, J.-M.; Heinly, J.; Zheng, E.; Dunn, E.; Fite-Georgl, P., and Pollefeys, M., 2013. Geo-registered 3D models from crowdsourced image collections. *Geo-spatial Information Science*, 16(1), 55–60.

Frantz, E.R.; Byrne, M.J., Sr.; Caldwell, A.W., and Harden, S.L., 2017. *Monitoring Storm Tide and Flooding from Hurricane Matthew along the Atlantic Coast of the United States, October 2016. U.S. Geological Survey Open-File Report 2017-1122,* 37p.

Goudarzi, M. and Landry, R., Jr., 2017. Assessing horizontal positional accuracy of Google Earth imagery in the city of Montreal, Canada. *Geodesy and Cartography*, 43, 56–65.

Hapke, C.J.; Himmelstoss, E.A.; Kratzmann, M.G.; List, J.H., and Thieler, E.R., 2010. *National Assessment of Shoreline Change: Historical Shoreline Change along the New England and Mid-Atlantic Coasts. U.S. Geological Survey Open-File Report 2010-1118,* 57p.

Harwin, S. and Lucieer, A., 2012. Assessing the accuracy of georeferenced point clouds produced via multi-view stereopsis from unmanned aerial vehicle (UAV) Imagery. *Remote Sensing*, 4(6), 1573–1599.

Hobbs, P.R.N.; Gibson, A.; Jones, L.; Pennington, C.; Jenkins, G.; Pearson, S., and Freeborough, K., 2010. Monitoring coastal change using terrestrial lidar. *Geological Society, London, Special Publications*, 345, 117–127.

Holman, R.A. and Stanley, J., 2007. The history and technical capabilities of Argus. The CoastView Project: Developing coastal video monitoring systems in support of coastal zone management *Coastal Engineering*, 54(6–7), 477–491.

Hugenholtz, C.H.; Whitehead, K.; Brown, O.W.; Barchyn, T.E.; Moorman, B.J.; LeClair, A.; Riddell, K., and Hamilton, T., 2013. Geomorphological mapping with a small unmanned aircraft system (sUAS): Feature detection and accuracy assessment of a photogrammetrically-derived digital terrain model. *Geomorphology*, 194, 16–24.

Isenburg, M., 2013. LASzip. *Photogrammetric Engineering & Remote Sensing*, 79(2), 209–217.

JALBTCX (Joint Airborne LIDAR Bathymetry Technical Center of Expertise), 2016a. *2010 US Army Corps of Engineers (USACE) Joint Airborne Lidar Bathymetry*. Technical Center of Expertise (JALBTCX) Southeast Lidar: Florida, Georgia, South Carolina, North Carolina. Department of Commerce (DOC), National Oceanic and Atmospheric Administration (NOAA), National Ocean Service (NOS), Office for Coastal Management (OCM), Charleston, South Carolina. https://coast.noaa.gov/dataviewer/#/lidar/search/where:ID=1070

JALBTCX, 2016b. *2016 USACE NCMP Topobathy Lidar: Florida East Coast. Technical Center of Expertise (JALBTCX) Southeast Lidar: Florida, Georgia, South Carolina, North Carolina*. U.S. Department of Commerce (DOC), National Oceanic and Atmo-

spheric Administration (NOAA), National Ocean Service (NOS), Office for Coastal Management (OCM), Charleston, South Carolina. https://coast.noaa.gov/dataviewer/#/lidar/search/where:ID=5185

JALBTCX, 2017. *2016 USACE Post-Matthew Topobathy Lidar: Southeast Coast (VA, NC, SC, GA and FL)*. Technical Center of Expertise (JALBTCX) Southeast Lidar: Florida, Georgia, South Carolina, North Carolina. U.S. Department of Commerce (DOC), National Oceanic and Atmospheric Administration (NOAA), National Ocean Service (NOS), Office for Coastal Management (OCM), Charleston, South Carolina. https://coast.noaa.gov/dataviewer/#/lidar/search/where:ID=5184

James, M.R. and Robson, S., 2012. Straightforward reconstruction of 3D surfaces and topography with a camera: Accuracy and geoscience application. *Journal of Geophysical Research—Earth Surface*, 117(F3), F03017.

James, T.D.; Murray, T.; Barrand, N.E., and Barr, S.L., 2006. Extracting photogrammetric ground control from lidar DEMs for change detection. *The Photogrammetric Record*, 21, 312–328.

Javernick, L.; Brasington, J., and Caruso, B., 2014. Modeling the topography of shallow braided rivers using Structure-from-Motion photogrammetry. *Geomorphology*, 213, 166–182.

Klemas, V.V., 2015. Coastal and environmental remote sensing from unmanned aerial vehicles: An overview. *Journal of Coastal Research*, 31(5), 1260–1267.

Levoy, F.; Garestier, F.; Froideval, L.; Monfort, O., and Poullain, E., 2016. Contributions of airborne topographic LiDAR to the study of coastal systems, Chapter 6. *In:* Baghdadi, N. and Zribi, M. (eds.), *Land Surface Remote Sensing in Urban and Coastal Areas*. Amsterdam: Elsevier, pp. 231–268.

Lim, S.; Thatcher, C.A.; Brock, J.C.; Kimbrow, D.R.; Danielson, J.J., and Reynolds, B.J., 2013. Accuracy assessment of a mobile terrestrial lidar survey at Padre Island National Seashore. *International Journal of Remote Sensing*, 34, 6355–6366.

Lindemer, C.A.; Plant, N.G.; Puleo, J.A.; Thompson, D.M., and Wamsley, T.V., 2010, Numerical simulation of a low-lying barrier island's morphological response to Hurricane Katrina. *Coastal Engineering*, 57(11–12), 985–995.

Liu, S.B.; Poore, B.S.; Snell, R.J.; Goodman, A.; Plant, N.G.; Stockdon, H.F.; Morgan, K.L.M., and Krohn, M.D., 2014. USGS iCoast—Did the coast change? Designing a crisis crowdsourcing app to validate coastal change models. *Proceedings of the Companion Publication of the 17th ACM Conference on Computer Supported Cooperative Work & Social Computing, CSCW Companion 2014. ACM* (Baltimore, Maryland), pp. 17–20.

Mancini, F.; Dubbini, M.; Gattelli, M.; Stecchi, F.; Fabbri, S., and Gabbianelli, G., 2013. Using unmanned aerial vehicles (UAV) for high-resolution reconstruction of topography: The structure from motion approach on coastal environments. *Remote Sensing*, 5(12), 6880–6898.

Matthews, N.A.; Noble, T.A., and Breithaupt, B.H., 2016. Close-range photogrammetry for 3D ichnology: The basics of photogrammetric ichnology. *In:* Falkingham, P.L.; Marty, D., and Richter, A. (eds.), *Dinosaur tracks—Next Steps*. Life of the Past series. Bloomington: Indiana University Press, 520p.

McCall, R.T.; Van Thiel de Vries, J.S.M.; Plant, N.G.; Van Dongeren, A.R.; Roelvink, J.A.; Thompson, D.M., and Reniers, A.J.H.M., 2010. Two-dimensional time dependent hurricane overwash and erosion modeling at Santa Rosa Island. *Coastal Engineering,* 57(7), 668–683.

Mohammed, N.Z.; Ghazi, A., and Mustafa H.E., 2013. Positional accuracy testing of Google Earth. *International Journal of Multidisciplinary Sciences and Engineering*, 4(6), 6–9.

Nayegandhi, A.; Brock, J.C.; Wright, C.W., and O'Connell, M.J., 2006. Evaluating a small footprint, waveform-resolving lidar over coastal vegetation communities. *Photogrammetric Engineering & Remote Sensing*, 72(12), 1407–1417.

NGS (National Geodetic Survey), 2016. *Hurricane Matthew: Rapid Response Imagery of the Surrounding Regions*. U.S. Department of Commerce (DOC), National Oceanic and Atmospheric Administration (NOAA), National Ocean Service (NOS), National Geodetic

Survey (NGS), Remote Sensing Division, Silver Spring, Maryland. http://geodesy.noaa.gov/storm_archive/storms/matthew/index.html

NOAA (National Oceanic and Atmospheric Association), 2018a. *Emergency Response Imagery*. https://storms.ngs.noaa.gov/.

NOAA, 2018b. *Hurricane Matthew Imagery*. https://geodesy.noaa.gov/storm_archive/storms/matthew/

NOAA, 2018c. *Coastal Imagery Viewer*. https://geodesy.noaa.gov/storm_archive/coastal/viewer/index.html.

NOAA, 2018d. *Digital Coast*. https://coast.noaa.gov/digitalcoast/data/

NOAA, 2018e. *Lidar Datasets at NOAA Digital Coast*. https://coast.noaa.gov/htdata/lidar1_z/

Paredes-Hernández, C.U.; Salinas-Castillo, W.E.; Guevara-Cortina, F., and Martínez-Becerra, X., 2013. Horizontal positional accuracy of Google Earth's imagery over rural areas: A study case in Tamaulipas, Mexico. *Boletim de Ciências Geodésicas*, 19(4), 588–601.

Pietro, L.S.; O'Neal, M.A., and Puleo, J.A., 2008. Developing terrestrial-LIDAR-based digital elevation models for monitoring beach nourishment performance. *Journal of Coastal Research*, 24(6), 1555–1564.

Ružić, I.; Marović, I.; Benac, Č., and Ilić, S., 2014. Coastal cliff geometry derived from structure-from-motion photogrammetry at Stara Baška, Krk Island, Croatia. *Geo-Marine Letters,* 34, 555–565.

Sallenger, A.H.; Krabill, W.B.; Swift, R.N.; Brock, J.; List, J.; Hansen, M.; Holman, R.A.; Manizade, S.; Sontag, J.; Meredith, A.; Morgan, K.; Yunkel, J.K.; Frederick, E.B., and Stockdon, H., 2003. Evaluation of airborne topographic lidar for quantifying beach changes. *Journal of Coastal Research*, 19(1), 125–133.

Schmid, K.A.; Hadley, B.C., and Wijekoon, N., 2011. Vertical accuracy and use of topographic LIDAR data in coastal marshes. *Journal of Coastal Research*, 27(6A), 116–132.

Sherwood, C.R.; Long, J.W.; Dickhudt, P.J.; Dalyander, P.S.; Thompson, D.M., and Plant, N.G., 2014. Inundation of a barrier island (Chandeleur Islands, Louisiana, USA) during a hurricane: Observed water-level gradients and modeled seaward sand transport. *Journal of Geophysical Research—Earth Surfaces*, 119(7), 1498–1515, 2013JF003069.

Smith, M.W.; Carrivick, J.L., and Quincey, D.J., 2016. Structure from motion photogrammetry in physical geography. *Progress in Physical Geography: Earth and Environment,* 40(2), 247–275.

Smith, M.W. and Vericat, D., 2015. From experimental plots to experimental landscapes: Topography, erosion and deposition in sub-humid badlands from Structure-from-Motion photogrammetry. *Earth Surface Processes and Landforms*, 40(12), 1656–1671.

Sopkin, K.L.; Stockdon, H.F.; Doran, K.S.; Plant, N.G.; Morgan, K.L.M.; Guy, K.K., and Smith, K.E.L., 2014. *Hurricane Sandy: Observations and Analysis of Coastal Change*. Reston, Virginia: U.S. Geological Survey, *Series No. 2014–1088)*, 54p.

Stewart, S.R., 2017. *Hurricane Matthew (AL142016) 28 September–9 October 2016*. *National Hurricane Center Tropical Cyclone Report*, National Hurricane Center, Miami, Florida.

Stockdon, H.F.; Doran, K.S., and Sallenger, A.H., 2009. Extraction of Lidar-based dune-crest elevations for use in examining the vulnerability of beaches to inundation during hurricanes. *In:* Brock, J.C. and Purkis, S.J. (eds.), *Coastal Applications of Airborne Lidar*. *Journal of Coastal Research*, Special Issue No. 53, pp. 59–65.

Stockdon, H.F.; Sallenger, A.H.; List, J.H., and Holman, R.A., 2002. Estimation of shoreline position and change using airborne topographic lidar data. *Journal of Coastal Research*, 18(3), 502–513.

Sturdivant, E.J.; Lentz, E.E.; Thieler, E.R.; Farris, A.S.; Weber, K.M.; Remsen, D.P.; Miner, S., and Henderson, R.E., 2017. UAS-SfM for coastal research: Geomorphic feature extraction and land cover classification from high-resolution elevation and optical imagery. *Remote Sensing*, 9(10), 1020.

Thoeni, K.; Giacomini, A.; Murtagh, R., and Kniest, E., 2014. A comparison of multi-view 3D reconstruction of a rock wall using several cameras and a laser scanner. *Proceedings of the International Archives of the Photogrammetry, Remote Sensing and Spatial Information Sciences 2014 ISPRS Technical Commission V Symposium* (Riva Del Garda, Italy), Volume XL-5, pp. 573–580.

Thompson, D.M.; Dalyander, P.S.; Long, J.W., and Plant, N.G., 2017. *Correction of Elevation Offsets in Multiple Co-Located Lidar Datasets. U.S. Geological Survey Open-File Report 2017-1031,* 10p.

Tonkin, T.N. and Midgley, N.G., 2016. Ground-control networks for image based surface reconstruction: An investigation of optimum survey designs using UAV derived imagery and structure-from-motion photogrammetry. *Remote Sensing*, 8(9), 786.

Tonkin, T.N.; Midgley, N.G.; Graham, D.J., and Labadz, J.C., 2014. The potential of small unmanned aircraft systems and structure-from-motion for topographic surveys: A test of emerging integrated approaches at Cwm Idwal, North Wales. *Geomorphology*, 226, 35–43.

Tsai, M.L.; Chiang, K.W.; Huagn, Y.W.; Lin, Y.S.; Tsai, J.S.; Lo, C.F.; Lin, Y.S., and Wu, C.H., 2010. The development of a direct georeferencing ready UAV based photogrammetry platform. *Proceedings of the 2010 Canadian Geomatics Conference and Symposium* (Calgary, Alberta, Canada), 5p.

Tuell, G.; Barbor, K., and Wozencraft, J., 2010. Overview of the coastal zone mapping and imaging lidar (CZMIL): A new multisensor airborne mapping system for the U.S. Army Corps of Engineers. *Proceedings of SPIE Defense, Security, and Sensing–Algorithms and Technologies for Multispectral, Hyperspectral, and Ultraspectral Imagery XVI* (Orlando, Florida), 76950R. doi: 10.1117/12.851905

Turner, I.L.; Harley, M.D., and Drummond, C.D., 2016. UAVs for coastal surveying. *Coastal Engineering*, 114, 19–24.

Turner, D.; Lucieer, A., and Wallace, L., 2014. Direct georeferencing of ultrahigh-resolution UAV imagery. *IEEE Transactions on Geoscience and Remote Sensing,* 52(5), 2738–2745.

USGS (U.S. Geological Survey), 2018a. *Flood Event Viewer*. Matthew 2016. https://stn.wim.usgs.gov/FEV/#MatthewOctober2016

USGS, 2018b. *Carolina Coastal Change Processes*. https://woodshole.er.usgs.gov/project-pages/cccp/public/COAWST.htm

van Verseveld, H.C.W.; van Dongeren, A.R.; Plant, N.G.; Jäger, W.S., and den Heijer, C., 2015. Modelling multi-hazard hurricane damages on an urbanized coast with a Bayesian Network approach, *Coastal Engineering*, 103, 1–14. doi: 10.1016/j.coastaleng.2015.05.006

Wang, Y.; Zou, Y.; Henrickson, K.; Wang, Y.; Tang, J., and Park, B.-Y., 2017. Google Earth elevation data extraction and accuracy assessment for transportation applications. *PLOS One*, 12(4), e0175756.

Warner, J.C.; Armstrong, B.; He, R., and Zambon, J.B., 2010. Development of a coupled ocean–atmosphere–wave–sediment transport (COAWST) modeling system. *Ocean Modelling*, 35(3), 230–244.

Warrick, J.A.; Ritchie, A.C.; Adelman, G.; Adelman, K., and Limber, P.W., 2017. New techniques to measure cliff change from historical oblique aerial photographs and structure-from-motion photogrammetry. *Journal of Coastal Research*, 33(1), 39–55.

Westoby, M.J.; Brasington, J.; Glasser, N.F.; Hambrey, M.J., and Reynolds, J.M., 2012. 'Structure-from-Motion' photogrammetry: A low-cost, effective tool for geoscience applications. *Geomorphology*, 179, 300–314.

Wheaton, J.M.; Brasington, J.; Darby, S.E., and Sear, D.A., 2010. Accounting for uncertainty in DEMs from repeat topographic surveys: Improved sediment budgets. *Earth Surface Processes and Landforms*, 35(2), 136–156.

White, S.A.; Jeong, I.; Hess, K.W.; Wang, J., and Myers, E., 2016. *An Assessment of the Revised VDATUM for Eastern Florida, Georgia, South Carolina, and North Carolina*. Silver Spring, Maryland: U.S. Department of Commerce, National Oceanic and Atmospheric Administration, National Ocean Service, *NOAA Technical Memorandum NOS 38,* 35p. https://vdatum.noaa.gov/download/publications/TM_NOS_CS38_FY17_White_VDatum_SAB_Update_Analysis.pdf

Wozencraft, J., 2017. JALBTCX Activities and USACE National Coastal Mapping Program Update. *Proceedings of the 18th Annual JALBTCX Airborne Coastal Mapping and Charting Workshop* (Savannah, Georgia), 31p. http://shoals.sam.usace.army.mil/Workshop_Files/2017/Day_01_pdf/d1s1b_Wozencraft.pdf

Wozencraft, J. and Millar, D., 2005, Airborne lidar and integrated technologies for coastal mapping and nautical charting. *Marine Technology Society Journal*, 39(3), 27–35.

Yates, M.L.; Guza, R.T., and O'Reilly, W.C., 2009. Equilibrium shoreline response: Observations and modeling. *Journal of Geophysical Research—Oceans*, 114(C9), 2156–2202, C09014.

Zhang, K.; Whitman, D.; Leatherman, S., and Robertson, W., 2005. Quantification of beach changes caused by Hurricane Floyd along Florida's Atlantic coast using airborne laser surveys. *Journal of Coastal Research*, 21(1), 123–134.